PCCP

PAPER

View Article Online
View Journal | View Issue

Cite this: *Phys. Chem. Chem. Phys.*, 2016, **18**, 8820

Competitive effects of oxygen vacancy formation and interfacial oxidation on an ultra-thin HfO_2-based resistive switching memory: beyond filament and charge hopping models†

Hisao Nakamura*[ab] and Yoshihiro Asai[b]

Received 10th February 2016,
Accepted 1st March 2016

DOI: 10.1039/c6cp00916f

www.rsc.org/pccp

We studied the quantum transport mechanism of an ultra-thin HfO_2-based resistive random access memory (ReRAM) cell with TiN electrodes and proposed the design of a sub-10 nm scale device. It is believed that formation and rupture of the conduction path in the local filament causes the switching between high and low resistive states. However, the validity of this simple filament model is not obvious in the sub-10 nm scale device because the redox processes occur mainly in a few nm range at the interface. Furthermore, the intrinsic transport mechanism of the device, in particular, quantum coherence, depends on device materials and length-scale. The relationship between the redox states and the transport mechanism like ballistic or hopping is still under debate when the device length scale is less than 10 nm. In the present study, we performed first-principles calculations of the non-equilibrium Green's function including electron–phonon interactions. We examined several characteristic structures of the HfO_x wire (nano-scale conduction path) and the interfaces between the resistive switching layer and electrodes. We found that the metal buffer layer induced a change in the oxygen-reduction site from the interface of HfO_x/TiN to the buffer layer. Even when the inserted buffer layer is a few atomic layers, this effect plays an important role in the enhancement of the performance of ON/OFF resistive switching and in the reduction of the inelastic electric current by electron–phonon scattering. The latter suppresses the hopping mechanism, which makes the ballistic conduction the dominant mechanism. We evaluated the activation energy in the high temperature limit by using the first-principles results of inelastic current. Our theoretical model explains the observed crossover of the temperature dependence of ReRAM cells and gives a new insight into the principle of operation on a sub-10 nm scale ReRAM device.

Introduction

Nonvolatile memory has become one of the major research targets in nanoelectronics because of society's need for low power devices, big data technology, and data-driven information processes. Resistive random access memory (ReRAM) is one of the most promising next-generation nonvolatile memory technologies and has been attracting increasing attention because of its capability for high-density integration as well as its fast and low power operation. However, the problematic issue of large variation in resistance values must still be resolved to enable the practical use of this technology.[1] The fundamental structure of the ReRAM cell is simple. The cell consists of two electrodes and a resistive switching layer (RSL) usually made of a transition metal oxide that is placed between the two electrodes. The filament model has been frequently used for the discussion of the ReRAM operation mechanism. The mechanism consists of two steps: (a) first, the filament is formed in the RSL during the fabrication process and (b) the filament is connected/disconnected to/from the electrode by oxygen (O_x) migration [oxygen vacancies (V_o)][2–4] in the ON/OFF switching operation that is sometimes called the SET/RESET process. This either creates or annihilates the current path. The thickness of the memory cell and the RSL has continuously decreased and is now below 10 nm and 5 nm, respectively, in order to enable low voltage read/write operation below 0.2 V.[5,6] While the switching of ReRAM is either unipolar or bipolar and usually depends on the RSL material, switching is exclusively bipolar when the thickness decreases well below 10 nm.[7] In such an ultra-thin RSL, the concept of the filament becomes

[a] *Research Planning Office, Department of Materials and Chemistry, National Institute of Advanced Industrial Science and Technology (AIST), 1-1-1 Umezono, Tsukuba Central 1, Tsukuba, Ibaraki, 305-8560, Japan. E-mail: hs-namaura@aist.go.jp*
[b] *Research Center for Computational Design of Advanced Materials, National Institute of Advanced Industrial Science and Technology (AIST), 1-1-1 Umezono, Tsukuba Central 2, Tsukuba, Ibaraki, 305-8568, Japan*

† Electronic supplementary information (ESI) available. See DOI: 10.1039/c6cp00916f

ill-defined and V_o migration predominantly occurs at the interface rather than in the filament. Thus, the filament model should be replaced by the unified redox model, where resistive switching occurs as the result of a redox reaction at the interface between the O_x donor (RSL) and the acceptor (electrode).[8] The unified redox model implicitly involves Schottky barrier modulation due to oxidation.

While the overall switching mechanism has been elucidated as described above, a microscopic description of the switching mechanism and the redox processes still remains an open question. Unfortunately, the roles of V_o distribution in the RSL and the oxidized interface for the ReRAM cell performance have been largely unexplored. Because of this, the electric transport and the switching mechanism connecting the high and low resistance states (HRS/LRS) remain a matter of strong debate. While some thermodynamic or kinetic models for the interfacial oxide free energy exist,[9,10] these are not very useful for the atomistic understanding and prediction of the current–voltage (*I–V*) characteristics. It should be stressed that the thickness of the RSL in the ReRAM cell has been reduced to the length scale around 10 nm, which is already well within the length regime where the quantum transport theory becomes necessary. Despite its rather phenomenological nature, the quantum point contact theory was tested in comparison with the observed *I–V* characteristics of the LRS.[11–13] However, the application of a high-quality quantum transport theory is necessary to obtain the microscopic understanding of the *I–V* characteristics of the ReRAM cell.

In the present study, we use the first-principles quantum transport simulation method to study the *I–V* characteristics of the ultra-thin HfO_2-based ReRAM cells. Because of their ease of fabrication, TiN electrodes are frequently used in experiments and were therefore used in our calculations as well. We focus on the studies of LRS and HRS in the low bias regime (typically up to 0.2 V) using the non-equilibrium Green's function theory calculations based on the density functional approximation (NEGF-DFT).[14] The impact of interfacial oxidation on the electric current ON/OFF ratio and the transport mechanism is discussed in terms of NEGF-DFT augmented by the electron–phonon coupling correction.

Computational model for the ultra-thin ReRAM cell

We introduce a structure model defined by the minimal unit cell consisting of a single HfO_2 wire, which relates to *c*-HfO_2 phase, and two (1×1) cubic TiN electrodes with the (001) interface. We call this minimal unit cell a "bin". To make the unit cell of a heterojunction consisting of HfO_2 and TiN, strain is imposed on each lattice constant. Within the present DFT calculations, the strain of *a* and *b* axes is 3% for HfO_2 and 13% for TiN, respectively. The strain of the *c*-axis imposed on TiN is 6% while that of HfO_2 is almost negligible. We note that the effect of the resulting strain of TiN electrodes is not important for the present purpose, *i.e.*, analysis of transport properties of HRS and LRS.[15] The HfO_2 part of the bin involves nine Hf layers corresponding to the thickness of around 2.2 nm. To model the electrodes, we include 14 layers of TiN for each of the two sides; thus, the total thickness of the cell is approximately 8.0 nm. Our device model for the TiN/HfO_x/TiN cell consists of four bins, *i.e.*, we use a supercell containing a bundle of 2×2 bins, as shown in Fig. 1. We investigate several possibilities for LRS of the ReRAM cell by removing some O atoms from the four bins. A single bin has three possible states, *i.e.*, "off" (no V_o), "$4V_o$" (formation of four V_o), and "$8V_o$" (formation of eight V_o), as shown in Fig. 1. We examine two possible LRS structures out of all possible states that can be obtained by combinations of the three possibilities of the single bin in the cell. One possible structure consists of four $4V_o$-bins, and we call this the L_1 cell model. The other structure has two $8V_o$-bins and two off-bins; we call this the L_2 cell model. In other words, L_1 consists of four O_x-reduced $HfO_{1.33}$ nanowires, and L_2 has two $HfO_{0.89}$ metallic nanowires. For HRS, a cell consisting of four off-bins is considered and is called the H_1 cell model. It is very important to keep the removed O atoms at the interface between HfO_2 and TiN electrodes, as shown in Fig. 1. This ensures that the model structure conserves the number of total atoms. This structural model explicitly takes into account the effect of the interfacial oxidation caused by O_x migration on the first-principles NEGF-DFT transport calculations.

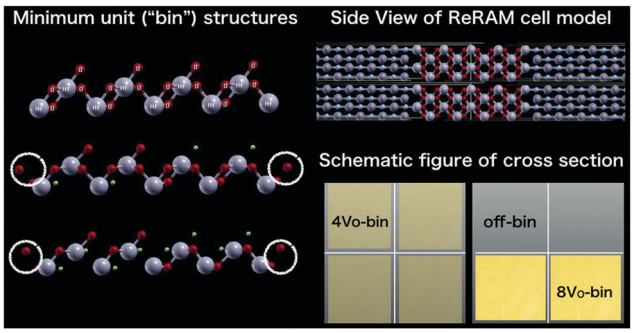

Fig. 1 (left) Minimum structures of HfO_2 nanowires (bins) of no V_o (upper panel), four V_o (middle panel), and eight V_o. Large grey and small red balls are Hf and oxygen atoms, respectively. Green balls represent the formation of V_o. The oxygen atoms labeled by white circles are migrated oxygen and oxidize the interface. (right) Structure of the ReRAM cell model. The upper panel represents the side view. Small dark grey and light blue balls are Ti and N atoms. The lower panel is the schematic figure of a cross-section of model RSL to represent the collocation of bins. The left side represents the L_1 model, *i.e.*, the V_o concentration is uniform in the cell. The right side represents the L_2 model and V_o concentration is locally accumulated.

To ensure that the bin model provides a reasonable structural model for the cell, we perform full optimization of the atomic geometry of the cell. The calculation results are summarized in Table S1 of the ESI,† and it can be seen that the bin model performs fairly well for the case of the O_x-reduced $HfO_{1.33}$ nanowire L_1 model. We also examine the L_2 cell model that includes the $HfO_{0.89}$ metallic wire. Here as well, the introduced geometry is stable against the optimization, demonstrating the validity of the bin model. We then use the present cell to evaluate the enthalpy difference between the two redox states given by $4V_o$-bin $\rightarrow$ $8V_o$-bin + oxidized. The calculated value is -0.54 eV, *i.e.*, the relative stabilities of the two states are comparable and the reaction can be energetically reversible. Thus, the bin

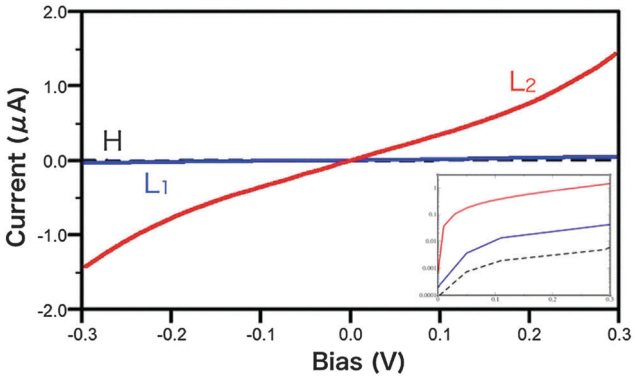

Fig. 2 The calculated *I–V* characteristics of ReRAM cells. The black dotted, blue, and red lines are *I–V* curves of H, L_1, and L_2 models, respectively. The inset shows the semi-log plot of the same *I–V* curves.

model provides a reasonable structural model that enables the study of the transport mechanism of the ReRAM cell using NEGF-DFT calculations.

The first-principles results of the *I–V* curve for the H_1, L_1, and L_2 cell models are summarized in Fig. 2. No differences between the electric current for one of the possible LRS and HRS represented by the L_1 cell model and the H_1 cell model can be seen in the figure, and the currents for the H_1 and the L_1 cell models are both small. In the previous study, we obtained a similar result for the comparison between the off-bins and the $4V_o$ single bins.[16] The observed similar results are reasonable because the atomic structure in the H_1 (L_1) cell model is close to a simple 2×2 multiplication of the single bin systems. On the other hand, the obtained electric current for the L_2 cell model is more than 10 times larger than that for the L_1 cell model, although the total amount of O deficiency within the cell is the same in these two cases. The results indicate that a local V_o accumulation is necessary to obtain a larger ON/OFF ratio. This may mean that a thicker (V_o-rich) conduction path (filament) is required. However, in both cases, the transmission probability around the Fermi energy E_F (we set E_F = 0.0 eV), *i.e.*, [−0.3 eV, 0.3 eV], is still small, below 0.1; thus, LRS is at best a poor metallic state. Because the band gap of the bulk $HfO_{1.33}$ is close to zero, our result may imply the formation of a barrier at the interface between the RSL and the electrode because of the oxidized interface originating from the migration of O_x. In the next section, we discuss this quantum point contact effect qualitatively.

Multi-layer ReRAM cell and point contact modulation by the oxidized interface

The insertion of a metal buffer layer can significantly affect the ReRAM cell properties. The metallic interlayer is usually used as an O_x scavenger and/or an acceptor in the SET process for the ReRAM cell,[17] and an insertion of the metal buffer layer may increase the O_x content in the RSL. Interfacial barrier reduction is another possible benefit of metal buffer layer insertion. The buffer layer insertion may protect the TiN electrode interface from the barrier formation because the barrier height formed at the metal buffer layer may be smaller than the barrier height formed at the TiN electrode interface. Both these possibilities can have a strong impact on the *I–V* characteristics of the ReRAM cell. We therefore investigate these effects using first-principles calculations by including the atomic buffer layer in our cell model. The metal buffer layer is denoted as M_B. A single atomic monolayer of tantalum is inserted at the interface between the RSL and the electrode. The monolayer insertion is made for both terminal interfaces of the RSL with the two electrodes. The resulting cell models are denoted as H_{1B}, L_{1B}, and L_{2B}, corresponding to their original H_1, L_1, or L_2 cells. The bin model and the construction method are then used to build the model structures for the monolayer-inserted cell.

We performed first-principles relaxation of atomic coordinates to determine the atomic geometries for the three bin states with the obtained structural parameters summarized in Table S1 of ESI.† The *I–V* curves for the cell models L_{1B} and L_{2B} are shown in Fig. 3. While the electric current for the H_{1B} cell model is quite small within the bias voltage range, similar to the case for the H_1 cell model, because of the M_B insertion, the electric current for the cell model L_{1B} is much larger than that for the L_1 cell. Because the V_o concentration and arrangement in the bins are fairly similar for the L_1 and L_{1B} cell models, this result suggests that the oxidized M_BO_x/TiN (L_{1B}) interface reduces the barrier height of the O_x-TiN/TiN (L_1) system, where O_x-TiN denotes the interfacial oxygen and the most outer TiN layer, *i.e.*, oxidized TiN surface. Our first-principles results support the hypothesis of barrier height reduction by buffer layer insertion. We also find that buffer layer insertion enhances the electric current in the case of the cell model L_{2B}, further supporting this hypothesis. The electronic coupling strength between the oxidized interface and the bulk electrode is estimated from the imaginary part of the complex eigenvalue of the effective molecular projected state Hamiltonian (MPSH).[18] The calculated values close to E_F are approximately 0.07 eV and 1.15 eV for O_x-TiN and M_BO_x, respectively, indicating that the contact resistance is smaller for the L_{1B} cell than for the L_1 cell. This directly demonstrates that the barrier height is reduced by buffer layer insertion. Both the barrier height and the filament

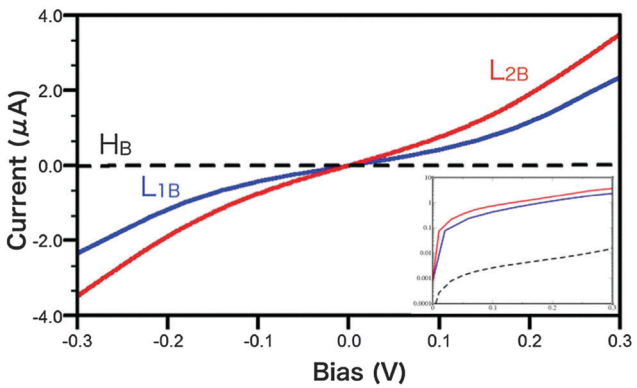

Fig. 3 The calculated *I–V* characteristics of ReRAM cells. The black dotted, blue, and red lines are *I–V* curves of H_B, L_{1B}, and L_{2B} models, respectively. The inset shows the semi-log plot of the same *I–V* curves.

thickness play important roles in controlling the *I–V* characteristics of the ReRAM cell. Therefore, the reduction of the barrier height in metal buffer layer cells found by our calculations can explain the experimentally observed improvement of the current ON/OFF ratio of the TiN/HfO_x/TiN cell upon insertion of the 5 nm-thick Hf buffer layer.[17,19] While there is a difference in the thicknesses of the buffer layers in our calculation and in the experiment, the physics underlying the effect of buffer layer insertion is common to both cases.

Electron–phonon interactions and temperature dependence

Experimentally, activation-type temperature dependence of the conductance has been observed for the ReRAM cell, suggesting a hopping conduction mechanism.[19,20] While this may cast some doubt on the applicability of the quantum transport theory,[21,22] buffer layer insertion dramatically reduces the temperature dependence; therefore, no temperature dependence is experimentally observed in this case.[17] This strongly suggests that the ballistic mechanism dominates the conduction. Below the thickness of 10 nm, the activation energy for the HfO_2-based ReRAM cell becomes as small as 0.05–0.10 eV,[17,19,20] enabling the description of the conduction with the quantum transport theory. To uncover the physics underlying these findings, it is necessary to use a theory that describes both the hopping and the ballistic transport mechanisms. Here we adopt the perturbation approach for the electron–phonon coupling effect. The most elaborate self-consistent theory for the electric and phonon currents including the electron–phonon coupling effects between them[23] describes the activation-type temperature dependence. We derived a scaling function from the calculation result obtained by using the self-consistent theory and a model Hamiltonian and found that it describes the experimental temperature dependence in the hopping regime.[24] The perturbation approach followed by the scaling function analysis is useful for the present study; however, here we adopt the first-principles lowest order expansion (LOE) theory, neglecting the phonon current, which is a reasonable choice for realistic computational resources.[14,25]

The plots of electric current *versus* bias voltage that include the electron–phonon coupling effect for the L_2 and L_{2B} cell models are shown in Fig. 4. To discuss the temperature (T) dependence, we use the plots at T = 25 K and at T = 50 K. Distinct temperature dependence is obtained for the two models. While the current increases with increasing temperature in the case of the L_2 model, no clear increase can be observed for the L_{2B} model. Fig. 5 shows the temperature dependent resistance R defined in terms of the inverse of the differential conductance at V = 0.1, *i.e.*, $R = (\mathrm{d}I/\mathrm{d}V)|_{V=0.1}{}^{-1}$. In this plot, the resistance is scaled by the resistance at T = 0 K. The resistance for the L_2 model decreases rather steeply with increasing temperature; therefore, as the temperature is increased from 50 K to 200 K, the resistance is reduced to approximately 20% of its original value. On the other hand, the temperature dependence for the L_{2B} model is much weaker, suggesting a larger role of the ballistic mechanisms for the conduction.

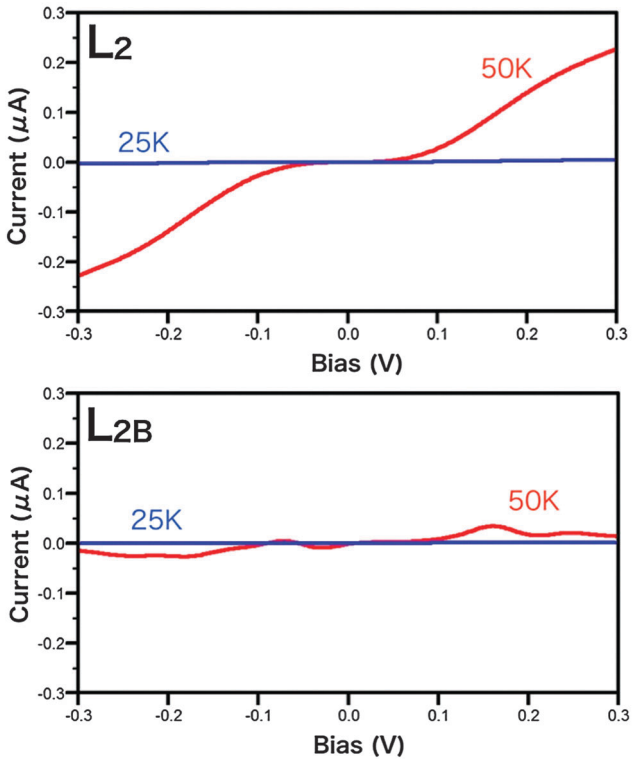

Fig. 4 Inelastic current–voltage characteristics at T = 25 K (blue) and 50 K (red). The upper panel shows the result of the L_2 cell and the lower panel shows the plot of the L_{2B} cell. Suppression of temperature dependence of inelastic current is found by comparing the two models.

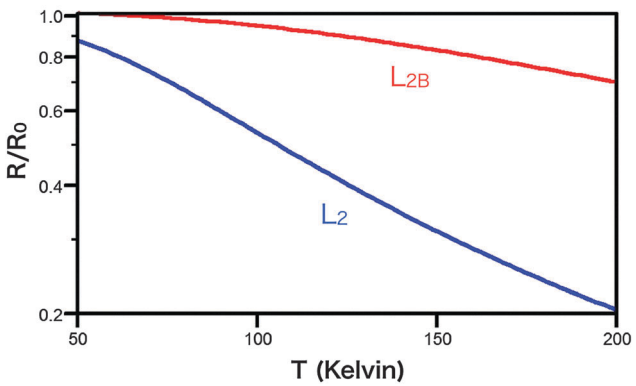

Fig. 5 The plot of the resistance of LRS (L_2 and L_{2B}) as a function of temperature. Each resistance value is normalized by that of the zero temperature limit.

Thus, the insertion of the buffer layer changes the conduction mechanism from hopping (L_2) to quasi-ballistic (L_{2B}).

We now discuss the reason for the reduction of the temperature dependence by buffer layer insertion. Within a simple single level model, the resistance ratio R/R_0 is given as follows:[26]

$$R/R_0 = 1 + (M^{\alpha})^{-2}\frac{\left\{(E_F - \varepsilon_C)^2+\gamma^2\right\}^2}{(E_F - \varepsilon_C)^2-\gamma^2}F(\Omega_\alpha, V, T) \qquad (1)$$

where ε_C and γ denote the site energy representing the energy of the conduction state and its coupling to the electrode, respectively. M_α and Ω_α denote the electron–phonon coupling strength and the phonon energy of the α-th phonon mode, respectively, and F is a negative function. The second term on the right-hand side is due to the electron–phonon coupling. While this term is negative and hence $R/R_0 < 1$ when γ is smaller than $|E_F - \varepsilon_C|$, it is positive and hence $R/R_0 > 1$ when γ is larger than $|E_F - \varepsilon_C|$. The former corresponds to the hopping mechanism and the latter corresponds to metallic conduction. This is essentially the same property with the 0.5 problem in inelastic tunneling spectroscopy (IETS):[27] while we obtain the dip IETS lineshape representing the resistance increase accompanying elastic electron–phonon scattering when the transmission τ is larger than 0.5, the peak IETS lineshape corresponds to the resistance decrease when τ is smaller than 0.5.[28] Because τ is given by $\tau = \gamma^2/[(E_F - \varepsilon_C)^2 + \gamma^2]$ in the simplest approximation, the 0.5 criterion corresponds to the criterion of γ being larger or smaller than $|E_F - \varepsilon_C|$. Because the theoretical MPSH analysis shows that γ is increased by the insertion of the buffer layer into the L cell, our theoretical result showing that the mechanism changes from hopping to metallic conduction with changes in the magnitude of γ is consistent with the experimental observation of the change due to buffer layer insertion. To compare with experiment, we estimate the activation energy E_a for the hopping conduction from the calculation results presented in Fig. 4 for the cell model L_2. We use the previously tested scaling function, given as $Ae^{-\tanh(B/T)} + C$, where A, B, and C are the fitting constants.[24,29] The fitting result is presented in Fig. 6 in the form of the normalized conductance denoted by g/g_0, and E_a is estimated to be approximately 0.03 eV from the fit. This is in reasonable agreement with the 0.05–0.10 eV E_a value experimentally estimated for the case where the thickness of the RSL is approximately two times larger than that of the RSL used in our calculations.[17,19,20]

To further check the validity of our modeling, we also estimate the activation energy E_a according to Marcus theory for the scenario of charge trap (*i.e.*, carrier localization) at the V_o site, which has often been adopted for ReRAM device simulation. We derive the Marcus parabola of the donor–acceptor states by injecting an electron charge into the V_o site. According to the theoretical study of polaron self-trapping at HfO_2 defects, V_o^{2-} is thermodynamically more stable than V_o^-.[30] We calculate the potential profile and estimate the activation energy. The obtained values for the V_o^{2-} state are 2.6 eV and 0.6 eV for the non-adiabatic limit and the adiabatic limit of charge transfer, respectively. These estimates are much higher than the experimentally estimated value. Even when the trapping state is assumed to be V_o^-, the activation energy values are 1.1 eV (non-adiabatic limit) and 0.4 eV (adiabatic limit), much further from the experimental result than the estimate obtained from Fig. 6.

We conclude that the NEGF-DFT method with the electron–phonon coupling correction is reasonably accurate for the study of the ReRAM cell below 10 nm thickness. We emphasize that the main difference between the electronic structures of the L_2 and L_{2B} models is the electronic coupling strength of the conduction state in the RSL with O_x-TiN and M_BO_x interfaces. The present results indicate that the change in the conduction mechanism from hopping to ballistic conduction caused by buffer layer insertion is explained within our theory.

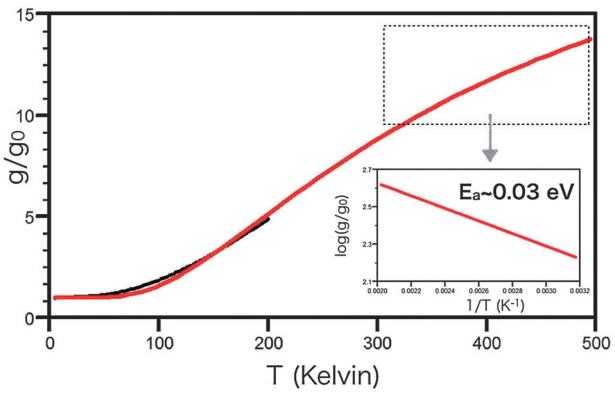

Fig. 6 The plot of the calculated normalized conductance (black line) and the fitted scaling function (red line). The dotted line is the region of [300, 500] K. The inset represents the plot of $1/T$ *vs* $\log(g/g_0)$ to check clearly whether temperature dependence is an activation type function or not.

Summary

Here we study the *I–V* characteristics of ultra-thin HfO_2-based ReRAM cells in the low-bias voltage regime using the quantum transport theory amended by the lowest order electron–phonon coupling correction. We describe the justification for this approach and examine several cell models focusing on the role of the oxygen vacancy (V_o) and the metal buffer layer insertion effect. The *I–V* calculations indicate that the local accumulation of V_o is crucial for the distinct energetically stable ON state. The electronic state of the oxidized contact by the SET process has a strong influence on the transport. The multi-layer cell structure obtained using metal buffer layer insertion is a promising approach to control the redox state at the interface accompanying the SET/REST operation. Our first-principles simulation predicts that the hybridization of conducting wavefunctions at the oxidized interface is crucial for obtaining distinct ON/OFF *I–V* behavior. We include the electron–phonon interaction effect into the non-equilibrium Green's function theory on the basis of density functional approximation and use it to study the temperature dependence of the resistance of the two low resistance states (LRS). Our results indicate that the electron–phonon coupling effect on the resistance is controlled by buffer layer insertion, with the conduction mechanism changing because of the insertion of the buffer layer. Thus, our study provides guidance for the design of the low-power operation of the ReRAM cell.

Method

All DFT calculations were performed using the SIESTA package,[31] and the NEGF-DFT transport calculations were then performed

using the HiRUNE subroutines developed in-house and interfaced with the SIESTA package.[14] We used the local density approximation (LDA) for the exchange–correlation (XC) functional and adopted the single zeta plus polarization function (SZP) level basis set for all atoms. We used 8 × 8 Monkhorst–Pack *k*-point sampling parallel to the surface direction. Full optimization of the atomic geometry in the cell was applied to the introduced bin models, and the result was compared with the structure obtained from the construction using the local structures of the four bins, *i.e.*, we compared the structures obtained with and without the construction. First, the distance between the two electrodes (L_{gap}) and the *a* and *b* lattice constants are optimized using the first-principles calculations, while the structure of each bin is fixed at the initial geometry. The lattice mismatch between the RSL and the electrode is taken into account within the optimization. Following this, the atomic geometries in the cells are determined by the calculation as all the atoms in the RSL and the two TiN layers closest to the surface are relaxed and optimized. We define the RSL thickness (L_{RSL}) as the distance between the two terminal Hf layers. The difference $L_{gap} - L_{RSL}$ corresponds to the thickness of the oxidized interface. All structural parameters are listed in the ESI.† To estimate the electronic coupling strength of the conducting RSL states and electrodes, we calculate the effective Hamiltonian using the NEGF-DFT results (see ESI†). The target state to evaluate the electronic coupling strength to the electrode is set to the interface, *i.e.*, $TiNO_2$ and Ta_2O_2 for with and without the Ta atomic layer, respectively. We evaluate the imaginary part of the elements of the last two terms in eqn (S2) (ESI†) to analyze the electronic coupling strength at the contact.

The electron–phonon coupling M^{α} is evaluated for each selected mode q_{α} by the numerical derivative as $\partial H/\partial q_{\alpha}$, where we consider only the Γ point for the phonon. We calculate the normal modes using the frozen phonon approximation and then select the localized modes in the RSL to evaluate electron–phonon couplings. The electric current is calculated using the NEGF framework with LOE, where 38 and 28 normal modes are explicitly included for L_2 and L_{2B}, respectively. For practical calculations of inelastic current using full NEGF-DFT, we adopt the lowest order expansion of Born approximation, which allows the same *k*-point sampling as that of ballistic transport calculations and the beyond-wideband-limit approximation, while avoiding computational difficulties. The detailed formalism is given in the ESI.†

The activation energy of the charge trap model was evaluated by the following a simplified constrained DFT procedure.[32] First, we consider two neighboring V_o sites in the RSL. To inject the trapped electron, we place a pseudo hydrogen (or helium) atom [*i.e.*, a pseudo ion + one/two electron(s)] at the position of one of the V_o and calculate the electron density matrix using the standard DFT technique. The resulting density matrix has the desired excess electron, *i.e.*, V_o^- or V_o^{2-} state in comparison with the original RSL. We calculate the Mulliken charge using the atomic orbital basis related to the pseudo atom and find that its value is −1.2 for V_o^- and −2.0 for V_o^{2-}. We fix the obtained density matrix and then recalculate the total energy of the original RSL using the same basis set, *i.e.*, the system consists of a RSL with an excess electron on the V_o site. We introduce a background positive charge to simulate the charge-doped RSL and perform the described procedure along the path of the V_o hopping sites. The resulting potential profile gives us the activation energy and the Marcus parabola.

Acknowledgements

H. N. and Y. A. acknowledge discussions and conversations with T. Miayzaki, H. Shima, and H. Akinaga. This work was supported by KAKENHI, a Grant-in-Aid for Scientific Research on Innovation Areas "Molecular Architectonics: Orchestration of Single Molecules for Novel Function" (#2511008). HN thanks the support of the Visiting Professorship Program at Institute for Catalysis, Hokkaido University.

References

1 H. Akinaga, Recent Advances and Future Prospects in Functional-Oxide Nanoelectronics: The Emerging Materials and Novel Functionalities that are Accelerating Semiconductor Device Research and Development. This is a translated version of the original paper which appeared in Oyo Buturi 81 (2012) 980 [in Japanese], 1–13, Doi: 10.7567/JJAP.52.100001 (2013).
2 D. H. Kwon, *et al.*, Atomic structure of conducting nanofilaments in TiO_2 resistive switching memory, *Nat. Nanotechnol.*, 2010, **5**, 148–153, DOI: 10.1038/Nnano.2009.456.
3 B. Magyari-Kope, M. Tendulkar, S. G. Park, H. D. Lee and Y. Nishi, Resistive switching mechanisms in random access memory devices incorporating transition metal oxides: TiO_2, NiO and Pr0.7Ca0.3MnO3, *Nanotechnology*, 2011, **22**, 254029, DOI: 10.1088/0957-4484/22/25/254029.
4 M. J. Lee, *et al.*, Electrical Manipulation of Nanofilaments in Transition-Metal Oxides for Resistance-Based Memory, *Nano Lett.*, 2009, **9**, 1476–1481, DOI: 10.1021/Nl803387q.
5 T. H. Hou, *et al.*, Evolution of RESET current and filament morphology in low-power HfO_2 unipolar resistive switching memory, *Appl. Phys. Lett.*, 2011, **98**, 103511, DOI: 10.1063/1.3565239.
6 A. Prakash, D. Jana and S. Maikap, TaO (x)-based resistive switching memories: prospective and challenges, *Nanoscale Res. Lett.*, 2013, **8**, 418, DOI: 10.1186/1556-276x-8-418.
7 T. Yanagida, *et al.*, Scaling Effect on Unipolar and Bipolar Resistive Switching of Metal Oxides, *Sci. Rep.*, 2013, **3**, 1657, DOI: 10.1038/srep01657.
8 H. Shima, H. Akinaga, Resistive Random Access Memory (ReRAM) Based on Metal Oxides, Special Issue of IEEE Proceedings "Nanoelectronics Research for Beyond CMOS Information Processing," 2010, 98, 2237–2251.
9 C. B. Lee, *et al.*, Effects of metal electrodes on the resistive memory switching property of NiO thin films, *Appl. Phys. Lett.*, 2008, **93**, 042115, DOI: 10.1063/1.2967194.

10 A. Makarov, V. Sverdlov and S. Selberherr, Stochastic model of the resistive switching mechanism in bipolar resistive random access memory: Monte Carlo simulations, *J. Vac. Sci. Technol., B: Nanotechnol. Microelectron.: Mater., Process., Meas., Phenom.*, 2011, **29**, 01ad03, DOI: 10.1116/1.3521503.

11 E. Miranda, A. Mehonic, J. Suñé and A. J. Kenyon, Multi-channel conduction in redox-based resistive switch modelled using quantum point contact theory, *Appl. Phys. Lett.*, 2013, **103**, 222904, DOI: 10.1063/1.4836935.

12 L. M. Prócel, *et al.*, Experimental evidence of the quantum point contact theory in the conduction mechanism of bipolar HfO_2-based resistive random access memories, *J. Appl. Phys.*, 2013, **114**, 074509, DOI: 10.1063/1.4818499.

13 C. Walczyk, *et al.*, Impact of Temperature on the Resistive Switching Behavior of Embedded HfO_2-Based RRAM Devices, *IEEE Trans. Electron Devices*, 2011, **58**, 3124–3131, DOI: 10.1109/Ted.2011.2160265.

14 H. Nakamura, K. Yamashita, A. R. Rocha and S. Sanvito, Efficient ab initio method for inelastic transport in nanoscale devices: Analysis of inelastic electron tunneling spectroscopy, *Phys. Rev. B: Condens. Matter Mater. Phys.*, 2008, **78**, 235420, DOI: 10.1103/PhysRevB.78.235420.

15 (*a*) Y. J. Oh, A. T. Lee, H. K. Noh and K. J. Chang, Hybrid functional *versus* quasiparticle calculations for the Schottky barrier and effective work function at TiN/HfO_2 interface, *Phys. Rev. B: Condens. Matter Mater. Phys.*, 2013, **87**, 075325, DOI: 10.1103/Physrevb.87.075325; (*b*) X. Zhong, *et al.*, The effect of a Ta oxygen scavenger layer on HfO_2-based resistive switching behavior: thermodynamic stability, electronic structure, and low-bias transport, *Phys. Chem. Chem. Phys.*, 2016, **18**, 7502–7510, DOI: 10.1039/C6CP00450D.

16 H. Nakamura, *et al.*, Design of ReRAM Cell Structure by Metal Buffer and Contact Engineering *via* First-Principles Transport Calculations, *2014 International Workshop on Computational Electronics (Iwce)*, 2014, DOI: 10.1109/IWCE.2014.6865829.

17 F. De Stefano, *et al.*, Nature of the filament formed in HfO_2-based resistive random access memory, *Thin Solid Films*, 2013, **533**, 15–18, DOI: 10.1016/j.tsf.2012.12.097.

18 H. Nakamura, Y. Asai, J. Hihath, C. Bruot and N. Tao, Switch of Conducting Orbital by Bias-Induced Electronic Contact Asymmetry in a Bipyrimidinyl-biphenyl Diblock Molecule: Mechanism to Achieve a pnDirectional Molecular Diode, *J. Phys. Chem. C*, 2011, **115**, 19931–19938, DOI: 10.1021/jp205723g.

19 F. De Stefano, *et al.*, Semiconducting-like filament formation in $TiN/HfO_2/TiN$ resistive switching random access memories, *Appl. Phys. Lett.*, 2012, **100**, 142102, DOI: 10.1063/1.3696672.

20 M. Wang, *et al.*, Thermoelectric Seebeck effect in oxide-based resistive switching memory, *Nat. Commun.*, 2014, **5**, 4598, DOI: 10.1038/ncomms5598.

21 W. J. Zhu, T. P. Ma, T. Tamagawa, J. Kim and Y. Di, Current transport in metal/hafnium oxide/silicon structure, *IEEE Electron Device Lett.*, 2002, **23**, 97–99, DOI: 10.1109/55.981318.

22 D. Ielmini, F. Nardi and C. Cagli, Resistance-dependent amplitude of random telegraph-signal noise in resistive switching memories, *Appl. Phys. Lett.*, 2010, **96**, 053503, DOI: 10.1063/1.3304167.

23 Y. Asai, Theory of local heating in single molecular bridge junctions, *Phys. Rev. B: Condens. Matter Mater. Phys.*, 2011, **84**, 085436, DOI: 10.1103/PhysRevB.84.085436.

24 Y. Asai, Theory of Electric Conductance of DNA Molecule, *J. Phys. Chem. B*, 2003, **107**, 4647–4652, DOI: 10.1021/jp027657m.

25 J. Viljas, J. Cuevas, F. Pauly and M. Häfner, Electron-vibration interaction in transport through atomic gold wires, *Phys. Rev. B: Condens. Matter Mater. Phys.*, 2005, **72**, 245415, DOI: 10.1103/PhysRevB.72.245415.

26 J. Hihath, *et al.*, Inelastic Transport and Low-Bias Rectification in a Single-Molecule Diode, *ACS Nano*, 2011, **5**, 8331–8339, DOI: 10.1021/Nn2030644.

27 M. Galperin, M. A. Ratner and A. Nitzan, Molecular transport junctions: vibrational effects, *J. Phys.: Condens. Matter*, 2007, **19**, 103201, DOI: 10.1088/0953-8984/19/10/103201.

28 T. Shimazaki and Y. Asai, Theoretical study of the lineshape of inelastic electron tunneling spectroscopy, *Phys. Rev. B: Condens. Matter Mater. Phys.*, 2008, **77**, 115428, DOI: 10.1103/Physrevb.77.115428.

29 S. K. Lee, *et al.*, Universal Temperature Crossover Behavior of Electrical Conductance in a Single Oligothiophene Molecular Wire, *ACS Nano*, 2012, **6**, 5078–5082, DOI: 10.1021/nn3006976.

30 D. M. Ramo, J. L. Gavartin, A. L. Shluger and G. Bersuker, Spectroscopic properties of oxygen vacancies in monoclinic HfO(2) calculated with periodic and embedded cluster density functional theory, *Phys. Rev. B: Condens. Matter Mater. Phys.*, 2007, **75**, 205336, DOI: 10.1103/Physrevb.75.205336.

31 J. M. Soler, *et al.*, The SIESTA method for *ab initio* order-N materials simulation, *J. Phys.: Condens. Matter*, 2001, **14**, 2745–2779, 2722.

32 N. Deskins and M. Dupuis, Electron transport *via* polaron hopping in bulk TiO_2: A density functional theory characterization, *Phys. Rev. B: Condens. Matter Mater. Phys.*, 2007, **75**, 195212, DOI: 10.1103/PhysRevB.75.195212.